Controlling the Cation Exsolution of Perovskite to Customize Heterostructure Active Site for Oxygen Evolution Reaction

Yicheng Wei,# Yao Zheng,# Yang Hu,# Mingzi Sun, Bolong Huang*, Pengfei Da, Pinxian Xi* and Chun-Hua Yan

KEYWORDS: Cation Exsolution; Perovskite oxide; Heterostructure; Oxygen evolution reaction; DFT calculation

ABSTRACT: Perovskite oxides are an important class of oxygen evolution reaction (OER) catalysts offering ordered atomic arrangement and highly flexible electronic structure. Currently, understanding and adjusting the dynamic reconstruction of perovskite during the OER process remains a formidable challenge. Here, we report the artificial construction of a heterostructure by the cation exsolution of perovskite to control the active site formation and reconstruction. The deliberately made La deficiency in $LaNiO_3$ perovskite facilitates the original segregation of NiO from the parent matrix and form a well-identified interface between perovskite crystal and NiO. The dynamic formation process of such heterojunction was studied by density functional theory computation and high quality imaging characterization. Due to the valence redistribution of Ni ions caused by the interfacial electron transfer, the *in-situ* formed $LaNiO_3$/NiO heterostructure displays a high d-band center to induce a strong electroactivity. Therefore, the $LaNiO_3$/NiO heterostructure exhibits a dynamic surface evolution feature with the generation of the highly active NiOOH layer under a low anodic potential (~1.35 V vs. RHE) during the OER process, which is very different from the conventional $LaNiO_3$ with a stoichiometry and NiO catalysts. With the newly formed heterostructure, the reconstructed catalysts impart a 4.5-fold increase in OER activity and a 3-fold improvement in stability against La and Ni dissolution during the OER process. This work provides a feasible interface engineering strategy for artificially controlling the reconstruction of the active phase in high-performance perovskite-based electrocatalytic materials.

INTRODUCTION

The electrocatalytic oxygen evolution reaction (OER) on the anode of water electrolyze limits the efficiency of the energy conversion process due to its sluggish four-electron transfer process.[1–4] One of the biggest challenges of OER is to develop highly efficient and stable catalysts. This triggered a search for OER electrocatalysts with earth-abundant elements such as 3d transition metal oxides. However, because of the anodic potential, the chemical composition and electronic properties of these oxides may inevitably be changed, leading to the surface self-reconstruction and generating new active species during the OER process.[5–10] This makes it difficult in understanding the intrinsic activity of the materials. Therefore the construction of controlled phase transition is the key to study the OER mechanism and develop new electrocatalysts.

Perovskite oxides (ABO_3) have been recently under the spotlight due to their ordered atomic arrangement and highly flexible electronic structure.[11–16] It is found that the original oxidation state of the catalytic material plays a crucial role in the formation of active site after the reconstruction.[17–23] Therefore, optimizing the electronic structure of perovskite by A-site or B-site substitution has been well demonstrated, such as B-site Fe substitution optimized Co-based perovskite oxide catalysts to form high-active surface amorphous oxyhydroxide layer.[17,18,20,23] Moreover, precise A-site Ce doping $LaNiO_3$ exhibits a dynamic reconstruction feature with the growth of a self-assembled NiOOH active layer during OER.[19] Therefore, the surface reconstruction of perovskite is beneficial to obtain a high activity. This makes it of great significance to in-depth understand the dynamic self-reconfiguration process and clarify the catalytic activity source of perovskite-based OER catalyst. However, how to rationally optimize the electronic structure of perovskite catalyst to regulate the reconstruction and obtain the target structure is still highly challenging.

Artificial construction of the heterogeneous structure is an efficient way to regulate the electronic property of oxides because the charge transfer between two phases and lattice stress often leads to new physical and chemical features.[24–27] Currently, most of the perovskite/oxide interfaces reported are prepared on substrates by physical deposition methods. The poor controllability leads to the ill-identified interfacial structure and weak electron transfer, which severely limits their practical application for activity enhancement. At the same time, in some nonstoichiometric perovskites, specific cations tend to segregate and form the interface between ABO_3 perovskite crystal matrix and exsolution content (AO or BO) under controlled thermal treatments.[28–30] Afterwards, the valence redistribution of cations is caused by the interfacial electron transfer, which significantly impacts the catalytic activities of the electrodes.

Herein, different from the previous mentioned strategies on pure-phase perovskite, a unique interface was constructed by an artificial exsolution method on a common $LaNiO_3$ perovskite. We introduce foreign compounds (i.e., NiO) onto the $LaNiO_3$ structure by deliberately controlling the composition proportion to tend the phase segregation in the parent perovskite. The in-situ formed the interface between $LaNiO_3$ perovskite crystal matrix and NiO exsolution content ($LaNiO_3$/NiO) shows unique electronic structures by attracting electrons from both $LaNiO_3$

and NiO bulks. Therefore, the $LaNiO_3/NiO$ heterostructure exhibits a dynamic surface evolution feature with the generation of a highly active NiOOH phase during the OER process, which brings an excellent activity and stability of the catalyst. This work offers the opportunities to customize heterostructure to prompt active phase transition for the further development of highly active perovskite catalysts.

RESULTS AND DISCUSSIONS

Heterostructure Evolution Process. A series of non-stoichiometric $LaNiO_3$ perovskites were prepared by a self-assembly synthesis method.[31] By deliberately inducing the La deficiency ($1 \leqslant R \leqslant 0.7$, R is defined as the molar ratio of La to Ni), we got a series of perovskite interfacial structures after annealing at 700 °C. The cubic Pm3m bunsenite structure for NiO is observed when $R < 1$ and the sample with $R = 0.8$ exhibits the optimum catalytic performance (Figure S1). On this sample ($R = 0.8$), XRD patterns were measured to investigate the phase transformation and intermediate states formed during the oxidation of La_2O_3/NiO heterostructure at different annealing temperatures. As shown in Figure 1a and Figure S2, La_2O_3/NiO heterostructure was firstly found below 550 °C. When the temperature increased to above 570 °C, the preferential growth of $LaNiO_3$ appeared to form $La_2O_3/LaNiO_3/NiO$ heterostructure. At a temperature of 700 °C, La_2O_3 was completely consumed and the $LaNiO_3/NiO$ heterostructure become thermally stable. We observe that have different X-ray absorption near-edge (XANES) of three heterostructure materials, the position is contributed by different valence states (La_2O_3/NiO < $La_2O_3/LaNiO_3/NiO$ < $LaNiO_3/NiO$). To further study the coordination structure of the Ni atom, the extended X-ray absorption fine structure spectroscopy (EXAFS) of these samples is transformed into R-space FFT ($K^3\chi$ (k)). It clearly shows that the bond length of Ni–O increases in the sequence of $LaNiO_3/NiO$ < $La_2O_3/LaNiO_3/NiO$ < La_2O_3/NiO. The results of XANES (Figure 1b and c) and X-ray photoelectron spectroscopy (XPS) (Figure 1d and S3) show that the interfacial electron transfer causes the redistribution of the valence states of Ni ions during the interface formation. Specifically, compared with $La_2O_3/LaNiO_3/NiO$ and La_2O_3/NiO, the banding energy of Ni 2p XPS spectra of $LaNiO_3/NiO$ displays a negative shift about 0.5 eV, which indicates a higher surface coupling and agrees well with the XANES result. In addition, O 1s XPS of $LaNiO_3/NiO$ also displays a kind of new active surface lattice oxygen ($O_{termination}$ and $O_{lattice}$, termination and lattice in perovskite) compared to the other two heterostructures (Figure 1d). Then, we have further compared catalytic performance, the $LaNiO_3/NiO$ heterostructure is demonstrated to exhibit the optimum (Figure S4).

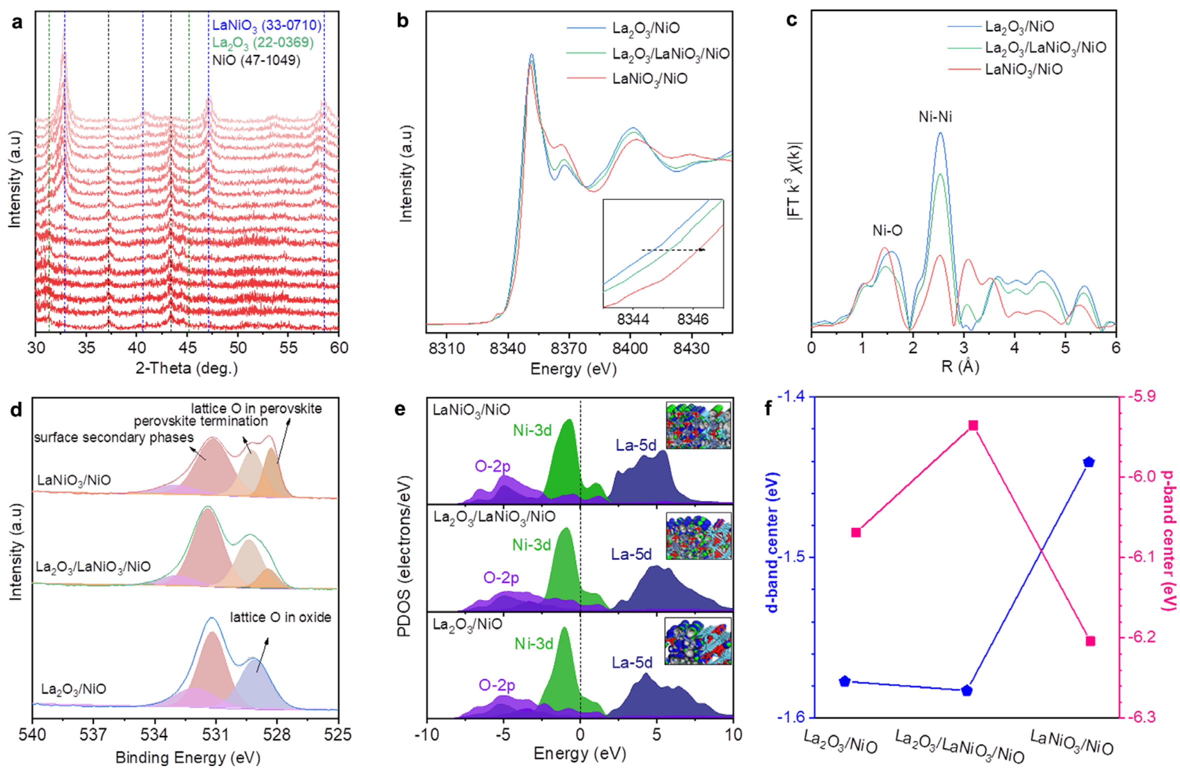

Figure 1. (a) The ex-situ XRD patterns on this sample ($R = 0.8$) measured at different temperatures. The diffraction peaks at 31.5° and 45.2° can be assigned to (400) and (440) of La_2O_3, 37.3° and 43.3° are (111) and (220) of NiO, and 32.8°, 47.3° and 52.9° are (110), (202) and (211) plane of $LaNiO_3$. (b) Ni K-edge XANES, (c) R-space Fourier-transformed FT (k^3 X(k)) and (d) XPS spectra of the O 1s region for La_2O_3/NiO (400 °C) $La_2O_3/LaNiO_3/NiO$ (580 °C) and $LaNiO_3/NiO$ (700 °C) samples. (e) The PDOS of proposed La_2O_3/NiO, $La_2O_3/LaNiO_3/NiO$ and $LaNiO_3/NiO$ structures. Inset shows the 3D contour plot of electronic distribution near E_F. Cyan balls = La, dark blue balls = Ni and red balls = O. Blue isosurface = bonding orbitals and green isosurface = anti-bonding orbitals. (f) The d-band center of Ni-3d and p-band center of O-2p in La_2O_3/NiO, $La_2O_3/LaNiO_3/NiO$, and $LaNiO_3/NiO$ heterostructures.

We have further applied density functional theory (DFT) calculation to investigate the dynamic formation and electronic structure of three different interfacial structures. First, all three heterostructures show the negative formation energies, indicating their stability during the synthesis (Figure S5). The increased formation energies are also consistent with the increased formation temperature during synthesis. Then, we have compared electronic distributions regarding the bonding and anti-bonding orbitals near the Fermi level (E_F) on the three different interface regions (Figure 1e). For La_2O_3/NiO and $La_2O_3/LaNiO_3$/NiO models, the distortions within the interfaces are evident. The electroactive regions still locate near the $LaNiO_3$ and NiO while La_2O_3 still shows the inert property. In comparison, the electronic distributions in $LaNiO_3$/NiO have been significantly activated in both $LaNiO_3$ and NiO. In particular, near the interface of $LaNiO_3$/NiO, we have noticed the major contribution of bonding orbitals, which indicates the electron-rich structures with high electroactivity. We further study the electronic structures regarding the projected partial density of states (PDOS) of three different interface structures (Figure 1e). For La_2O_3/NiO, Ni-3d and La-5d orbitals display overlapping with O-2p orbitals, leading to a stable structure. With the formation of the $LaNiO_3$, the electronic structures have not been significantly affected. However, for $LaNiO_3$/NiO it is noted that the dominant peak of the Ni-3d orbitals has slightly upshifted with improved electroactivity than La_2O_3/NiO and $La_2O_3/LaNiO_3$/NiO, which plays as the active sites for fast electron transfer with low energy barriers. In addition, we notice the appearance of an evident peak in O-2p orbitals near E_V = -4.98 eV on the $LaNiO_3$/NiO, which is slightly lower than of La_2O_3/NiO and $La_2O_3/LaNiO_3$/NiO, supporting a more electron-rich feature. Both these two features result in a higher valence state of Ni sites to promote the OER process. Moreover, the d-band center and p-band center in different heterostructures have been compared (Figure 1f). The d-band center of La_2O_3/NiO and $La_2O_3/LaNiO_3$/NiO heterostructures are barely changed while $LaNiO_3$/NiO shows an obviously upshifted d-band center. In the meantime, the p-band center of O in $LaNiO_3$/NiO exhibits the lowest p-band center, supporting the most electron-rich properties among the three samples. This agrees well with the charge density difference and PDOS analysis. DFT calculations have also confirmed the improved OER performances (Figure S6). For the rate-determining step of O* to OOH*, $LaNiO_3$/NiO delivers a much smaller energy barrier of 1.40 eV than that of La_2O_3/NiO and $La_2O_3/LaNiO_3$/NiO. This leads to much reduced overpotential of OER. In comparison, La_2O_3/NiO and $La_2O_3/LaNiO_3$/NiO show much overpotential, confirming the superior electroactivity of $LaNiO_3$/NiO heterostructures.

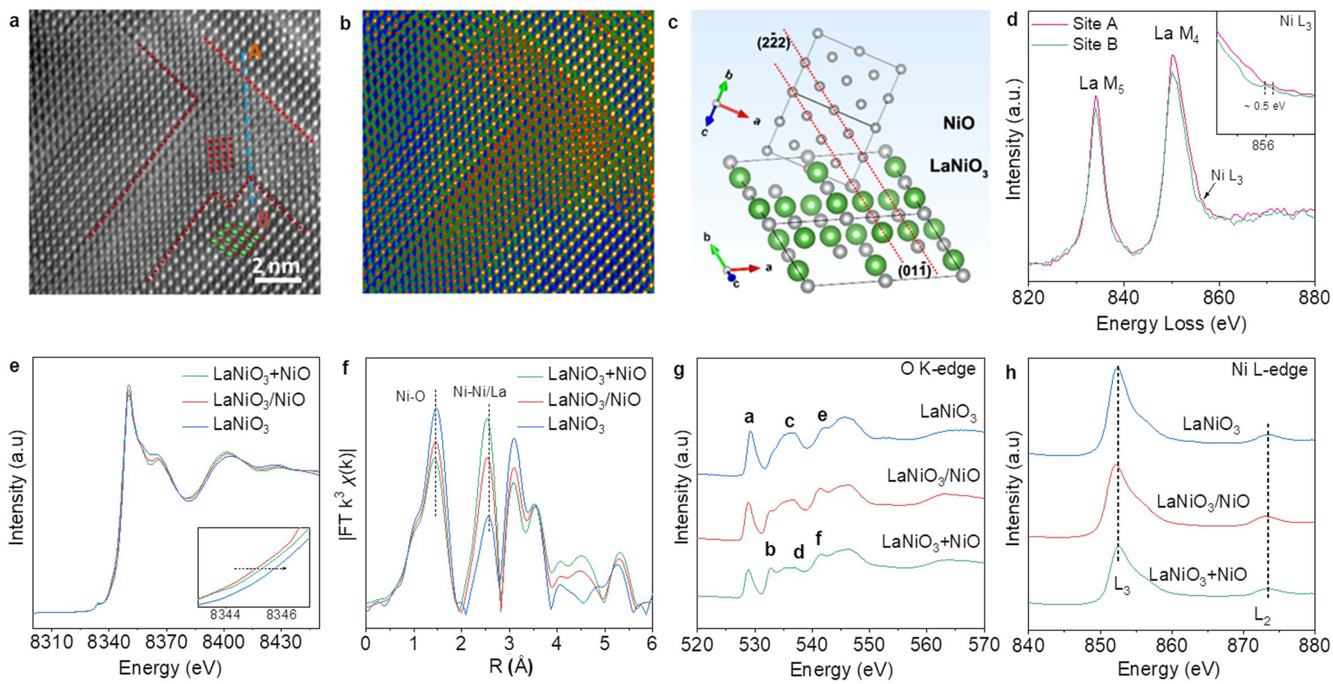

Figure 2. (a) Atomic HAADF-STEM image and (b) FFT-filtered image of $LaNiO_3$/NiO with a [011] orientation. (c) The crystal structure of the $LaNiO_3$ and NiO proposed based on the HAADF-STEM image. (d) The EELS spectra correspond to different positions (A, B, shown in Figure S10). (e) Ni K-edge XANES and (f) R-space Fourier-transformed Ni K-edge EXAFS for different catalysts. The soft X-ray absorption spectra of (g) O K-edges, and (h) Ni L-edges for different catalysts. In Figure 2g, peak **a, b** can be assigned as the overlapping band between Ni 3d and O 2p in $LaNiO_3$ and NiO, respectively; peak **c** is considered to be a superoxide species O^{2-} on the surface $LaNiO_3$; peaks **e** and **f** can be considered as the hybridization between O 2p and La 5d/Ni 4sp.

Local $LaNiO_3$/NiO Heterostructure Elucidation. According to the XRD patterns (Figure S7a), the $LaNiO_3$/NiO heterostructure displays two sets of crystal structure, involving hexagonal perovskite structure for $LaNiO_3$[32,33] and cubic Pm3m bunsenite structure for NiO[34]. Transmission electron microscopy (TEM) showed that $LaNiO_3$/NiO appeared as nanoparticles with an average size of 100 nm (Figure S7b), consistent with the same structure of pure $LaNiO_3$ (Figure S8b). The high-angle annular dark-field scanning transmission electron microscopy (HAADF-STEM) image revealed that the fine heterostructure of $LaNiO_3$/NiO can be identified as a constructed by $LaNiO_3$ perovskite structure with [011] orientation and additional NiO structure with [011] orientation (Figure 2a); NiO nanopillars are embedded in the $LaNiO_3$ matrix with {100}NiO//{100}$LaNiO_3$ as their interface (Figure 2c). Fast Fourier Transform-Filter (FFT-Filter) atomic resolution image was further utilized to visualize domain transformation (Figure 2b). The FFT patterns show the coexistence of two clearly distinct structural domains in the $LaNiO_3$ and NiO area (Figure S9a). And the corresponding line intensity profiles (Figure S9b) can directly display different periodic atomic arrangements in the two sides of the interface, which confirms that the introduction of heterogeneous interfaces leads to changes in the bonding mode of metal cations. Electron energy loss spectroscopy spectra (EELS) were further applied to understand the electronic information of Ni at the interface, which performed line scan on the interface along the red arrow in Figure S10. The results of EELS (Figure 2d) demonstrate that a 0.5 e^- negative charge is required to compensate polarity of the $[NiO_2–LaO]_{LaNiO3}–[Ni–O]_{NiO}$ interface.[35,36] It shows that NiO acquired some electrons from $LaNiO_3$ to form an electron-rich property, which is consistent with the DFT calculation results. In addition, the results of the depth profile of various secondary ion species (Figure S11) demonstrate the distribution of NiO in the $LaNiO_3$/NiO bulk phase. These results also prove the successful incorporation of NiO heterointerface in $LaNiO_3$ perovskite.

Electronic Structure Analysis. To better study interface interaction in $LaNiO_3$/NiO heterostructure, physically mixed $LaNiO_3$ + NiO sample was prepared as a reference. The XANES shows a slight valence redistribution of Ni ions induced by interfacial electron transfer $LaNiO_3$ + NiO and $LaNiO_3$/NiO (Figure 2e), which is further supported by XPS results showing an increased concentration of Ni^{2+} species in $LaNiO_3$/NiO heterostructure (Figure S12). In the EXAFS (Figure 2f), the bond length of Ni–O bond increases in the sequence of $LaNiO_3$ + NiO < $LaNiO_3$/NiO < $LaNiO_3$, which can be attributed to the distortion of the structure caused by the interface formed. In addition, Ni–Ni bond for $LaNiO_3$/NiO (ca. 2.52 Å) is shorter than that of $LaNiO_3$ + NiO (ca. 2.53 Å) and single-phase NiO (ca. 2.56 Å, Figure S13). This can be explained that the chemical recombination changes the electronic structure of the Ni–Ni bond in NiO owing to a strong interface interaction. In line with the Fourier transforms, the wavelet transform (WT) images reveal a reduced Ni–Ni path in $LaNiO_3$/NiO heterostructure than that of $LaNiO_3$ + NiO (Figure S14).

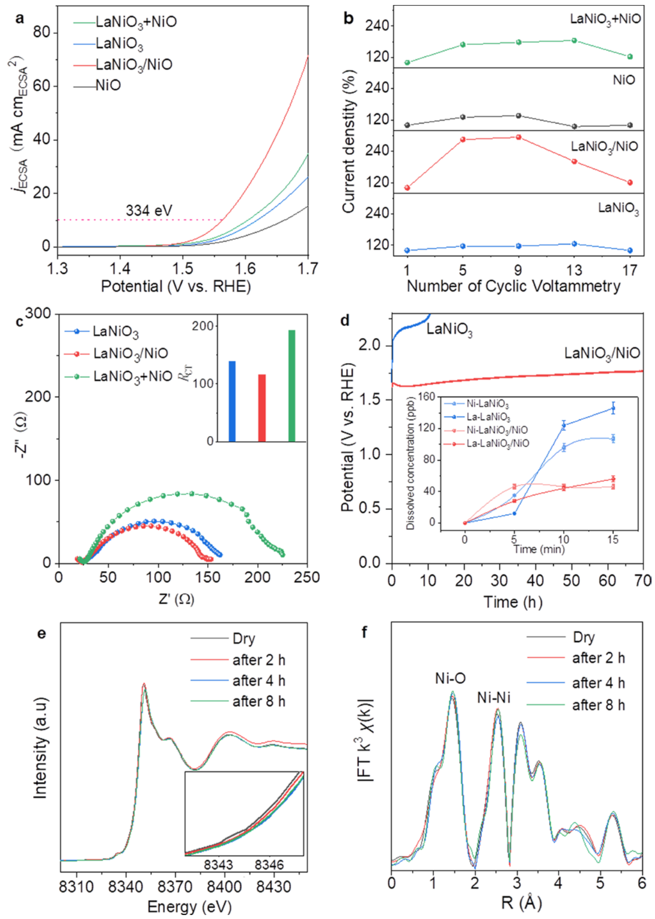

Figure 3. (a) The *iR*-corrected LSV curves from 10^{th} CV curves of different samples. (b) The CV in the potential region of 1.125 – 1.725 V vs. RHE for different samples. (c) EIS of different samples at a positive potential of 1.62 V versus RHE. (d) Chronoamperometric response of the $LaNiO_3$/NiO at 10 mA cm^{-2} current density for OER. Inset: Contents of leached metals in the electrolyte in the presence of $LaNiO_3$ and $LaNiO_3$/NiO during 15 min long electrocatalysis. (e) Ni K-edge XANES. Inset: adsorption edges. (f) R-space Fourier-transformed FT (k^3 X(k)) of Ni K-edge EXAFS of $LaNiO_3$/NiO catalysts on carbon papers after the operation of OER instantly at 1.6 V during 2 h, 4 h and 8 h.

The O 1s XPS spectra of different samples were also fur fitted into various oxygen species (Figure S15).[37–39] Notably, NiO's surface lattice oxygen fuses with perovskite's termination lattice to form a new kind of surface lattice oxygen in the $LaNiO_3$/NiO chemical interface (binding energy = 529.18 eV), which enhances the electron transfer between the two phases and reduces the hybrid state of Ni 3d and O 2p. The soft X-ray absorption spectra are further analyzed to reflect such orbital hybridization.[40–42] Compared with $LaNiO_3$ and $LaNiO_3$+NiO, $LaNiO_3$/NiO shows a narrowed hybrid orbit between Ni 3d and O 2p and their absorption peak (O p–band center) obviously shifts to a lower-energy position. The formation of $LaNiO_3$/NiO heterostructure reduces the covalency of the Ni–O bond and brings the center of O p-band closer to the E_F (Figure 2g). In addition, Ni L-edge XANES shows that L_3 in $LaNiO_3$/NiO heterostructure is not split and moves in the direction of lower energy, indicating that electron transfer between two phases changes e_g orbit position in Ni 3d (Figure 2h). All the above results suggest that interface electron transfer leads to redistribution in the valence state of Ni ions.

Electrochemical OER Activity. Electrochemical measurements were then performed on different samples with and without heterostructures. The $LaNiO_3/NiO$ heterostructure has an expected high OER current density with the overpotential of 334 mV (at 10 mA cm^{-2}), which is further supported by LSV normalized by catalysts' surface areas (Figure 3a). Additionally, the $LaNiO_3/NiO$ also shows an expected highest geometric area current density with the smallest Tafel slope, demonstrating the fastest OER kinetics on $LaNiO_3/NiO$ heterostructure (Figure S16a and b). These results clearly indicate that this unique heterostructure (i.e. electron-rich) is one of the main reasons for the enhanced activity of the highly active NiOOH species reconstructed after CVs. This process can be clearly reflected by multiple CV scans, $LaNiO_3/NiO$ (the biggest increase 194.1%) is activated, in contrast to $LaNiO_3$ (the biggest increase 25.1%) and NiO (the biggest increase 36.5%), which underwent little change (Figure 3b and S17).

Electrochemical impedance spectroscopy (EIS) was carried out to examine the electrical charge transfer behavior different phases[43–46] The results of EIS (Figure 3c, S18 and Table S4) show that the charge-transfer resistances of the $LaNiO_3/NiO$ declines considerably the smallest in comparison with that of $LaNiO_3$, $LaNiO_3$ + NiO and NiO. And the conventional four-probe technique was further evidence that the resistivity of the $LaNiO_3/NiO$ heterostructure declines considerably the smallest (Figure S19). This significant reduction in the charge-transfer barrier at the interface is one of the main reasons for the high OER activity of $LaNiO_3/NiO$. Meanwhile, the higher double-layer capacitance (C_{dl}) substantiates the larger electrochemical active area of $LaNiO_3/NiO$ than other samples (Figure S20).

Corrosion Resistance in OER. The long-term stability of $LaNiO_3/NiO$ catalyst under highly corrosive and oxidative conditions was investigated by a constant current chronopotentiometry at a current density of 10 mA cm^{-2} (Figure 3d). The $LaNiO_3/NiO$ heterostructure provides long continuous OER electrocatalysis over 70 h. The multipotential electrochemical stability measurement shows the robust stability of $LaNiO_3/NiO$ heterostructure for about 32 h-long multi-potential electrolysis (Figure S21). The leached amounts of cations during OER are quantitatively determined by inductively coupled plasma mass spectrometry (ICP-MS). For the $LaNiO_3/NiO$ heterostructure, the La and Ni dissolutions increase steadily at the first five minutes and then become constant. And the constant concentrations of La and Ni ions in the electrolyte are 28 and 46 ppb, respectively. The cation leaching for $LaNiO_3/NiO$ heterostructure is much weaker than that for $LaNiO_3$, which gives constant La and Ni concentrations of 107 and 146 ppb, respectively, in the electrolyte. This comparison suggests that the interfacial structure markedly enhances the structural stability of the latter.

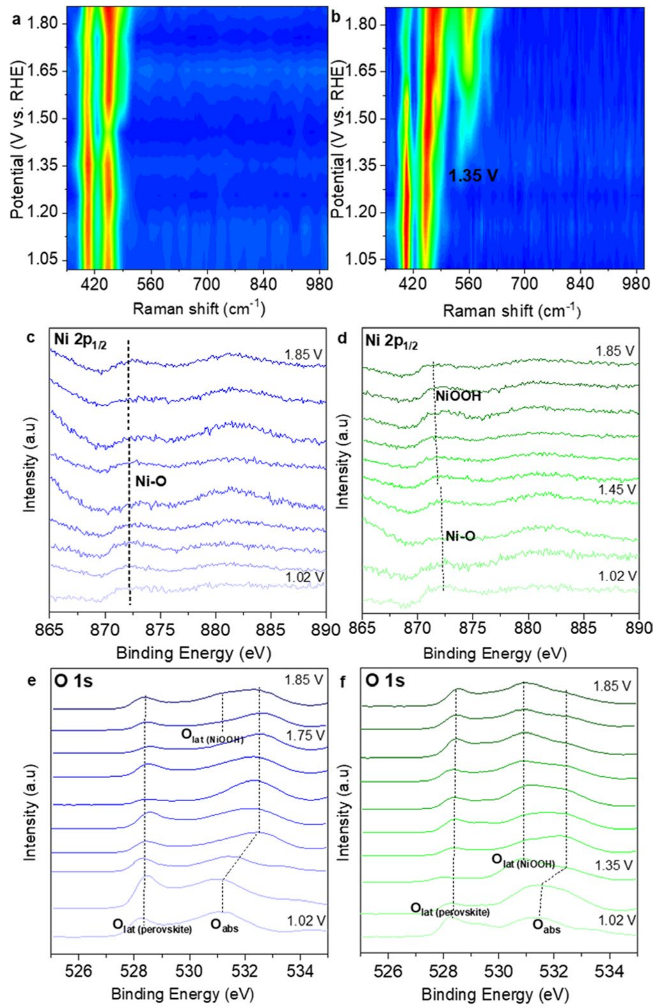

Figure 4. Potential-dependent operando Raman spectra of (a) $LaNiO_3$, (b) $LaNiO_3/NiO$. The pair of peaks at 400.6 and 450.4 cm^{-1}, which are attributed to the Ni–O vibrations of $LaNiO_3$, and at 474 (e_g) and 551 (A_{1g}) cm^{-1} can be assigned to the Ni–O bending and stretching vibrations of NiOOH. *Quasi in-situ* Ni 2p and O 1s XPS spectra for (c, e) $LaNiO_3$, and (d, f) $LaNiO_3/NiO$ at specific potential from 1.02 V to 1.85 V (vs. RHE).

After the catalytic test, we re-examined the chemical environment of the reconstructed $LaNiO_3/NiO$ phase during the OER process. The HRTEM image of post-8 h $LaNiO_3/NiO$ shows a continuous amorphous shell of about 1 nm (Figure S22). Additionally, the TEM image and corresponding EDS elemental mapping images of post-8 h $LaNiO_3/NiO$ nanoparticle show a more obvious outside shell (Figure S23). According to the HAADF-STEM images (Figure S24), this catalyst still maintains the original crystal structure. Furthermore, the XANES and X-ray absorption edges underwent little change and finally reach a steady state with the passage of OER time (Figure 3e and f), indicating that the apparent oxidation state of the Ni atom inevitably oxidizes during the OER process. In addition, the O K-edge XAS (Figure S25a) and Ni L-edge XANES spectrum (Figure S25b) move in the direction of lower energy, indicating that electron transfer between phases changes e_g orbit position in Ni 3d. These experimental results confirm that the formation of the active phase reduces the covalency of the Ni–O bond and brings the center of the O p-band closer to the E_F.

Identification of Active Sites. In order to directly identify the surface reconstruction process, operando Raman spectroscopy was employed under operating potentials. It clearly shows that the $LaNiO_3$ and NiO substantially retain the structure; NiOOH species were detected until the potential of ~ 1.75 V and 1.55 vs. RHE, respectively (Figure 4a and S26a).[47–49]. In sharp comparison, the $LaNiO_3$/NiO sample with an electron-rich heterostructure can evolve into NiOOH completely under a low potential of ~1.35 V vs. RHE (Figure 4b and S26b). Such evidence agrees well with previous XAS and calculation analysis of Ni electron transfer, also consistent with the results of CVs.

The near-surface electronic structure was also investigated by quasi in-situ XPS during OER. It clearly shows that the Ni $2p_{1/2}$ of $LaNiO_3$ and NiO retains until the potential achieves at 1.85 V vs. RHE (Figure 4c and S27a). By contrast, the Ni $2p_{1/2}$ of $LaNiO_3$/NiO is obviously shifting to lower energies under a low potential of ~1.45 V vs. RHE (Figure 4d), consistent with operando Raman results. In the O 1s spectra, $LaNiO_3$/NiO appear significant new peaks at approximately 531.0 eV in under a low potential of ~1.35 V vs. RHE (Figure 4f), which is different from that of $LaNiO_3$ (~ 1.75 V, Figure 4e) and NiO (~ 1.55 V, Figure S27b). This feature can indicate the presence of surface chemisorbed oxygen such as O_2^{2-} or O^-, which belongs to hydroxyl-like groups (e.g. NiOOH).[50,51] By combining the above operando results, it was found that the $LaNiO_3$/NiO heterostructure could significantly promote the formation of an active self-constructed surface NiOOH layer during the OER process, which boosted the OER performance.

DFT Calculations of electron transfer through $LaNiO_3$/NiO. Considering the complicated interface structures in $LaNiO_3$/NiO, DFT calculated site-dependent PDOS was used to reveal the detailed electronic structures (Figure 5a). Notably, Ni sites have shown distinct electronic structure evolutions in different regions of the heterostructure. Within the NiO and interface, Ni-3d orbitals display the upshifting trend towards the Fermi level from bulk to the surface, leading to smaller electron transfer barriers with increased valence states and improved electroactivity. The O-2p states also display different electronic behaviors, where the O-2p states of the interface are more electroactive than the NiO due to closer distance to the E_F (Figure 5b). O-2p orbitals in $LaNiO_3$ demonstrate the highest p-band center, which is well preserved from bulk to the surface. These electronic structures reveal that the active sites are mainly located at the Ni sites at the IF. During the oxidation environment of OER, the formation of NiOOH at the interface and surface NiO becomes easier due to the reduced energy barrier. which is consistent with the experimental results. As shown in Figure 5c, such electron transfer pathways and different valance states in different regions of $LaNiO_3$/NiO can be validated by experimental CVs. As shown in Figure 5d, there is no obvious Ni^{2+}/Ni^{3+} redox in the curve of individual NiO, indicating it is hard to be oxidized. Such observation was also found on $LaNiO_3$. Conversely, the $LaNiO_3$/NiO heterostructure catalyst exhibits early oxidation peaks of the Ni^{2+}/Ni^{3+} redox (1.35 V) than the $LaNiO_3$ standalone counterpart (1.37 V), supporting a more electron-rich feature as proposed by the PDOS analysis.

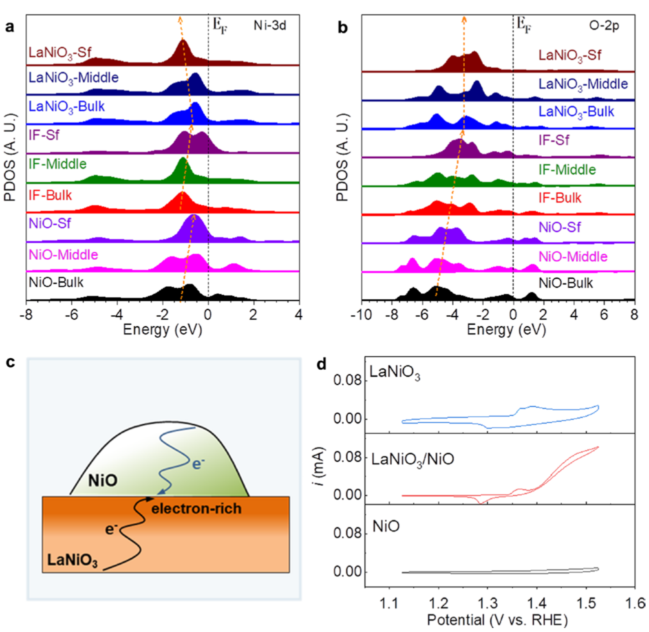

Figure 5. The site-dependent PDOS of (a) Ni-3d and (b) O-2p in $LaNiO_3$/NiO different sites. (c) Schematic diagram of charge transfer process through the bulk to the interface of $LaNiO_3$/NiO. (d) The CV in the potential region of 1.125 – 1.525 V vs. RHE for different samples.

CONCLUSIONS

In summary, we have successfully developed a unique electron-rich $LaNiO_3$/NiO heterostructure by controlling the composition proportion through the B-sites exsolution method. The formation of $LaNiO_3$/NiO interfacial structure optimizes the O 2p level of the catalyst to obtain greater structural flexibility, which promotes the surface reconstruction into the highly active NiOOH phase so as to improve the OER activity and stability. DFT calculations have compared the distinct electronic environments in the heterostructures, where the Ni sites demonstrate converse evolutions in NiO and $LaNiO_3$. The Ni sites in the IF show high electroactivity and lead to the formation of NiOOH. Therefore, this works provides a promising way to facilitate the generation of active phases by interface controlling strategy.

METHODS

Chemical Materials: Ni $(NO_3)_2 \cdot 6H_2O$, $La(NO_3)_3 \cdot 6H_2O$, ethylene diamine tetraacetic acid ($C_{10}H_{16}N_2O_8$), citric acid monohydrates ($C_6H_8O_7 \cdot H_2O$), HNO_3 (CR) and KOH, commercial iridium carbon catalyst (20 wt%), and Nafion® (5 wt%) were purchased from Aladdin. The commercial carbon paper was purchased from Fuel Cell Store. All the standard solutions were prepared with Milli-Q water with a resistance of 18 MΩ cm. All gases (argon, oxygen) were of 5N quality (99.999%, Airgas).

Materials synthesis: The $LaNiO_3$ was synthesized using a sol-gel method.[31] 2 mmol $La(NO_3)_3 \cdot 6H_2O$, 2 mmol $Ni(NO_3)_2 \cdot 6H_2O$ were dissolved in deionized (DI) water, 8 mmol ethylene diamine tetraacetic acid ($C_{10}H_{16}N_2O_8$) and 5 mmol citric acid monohydrates ($C_6H_8O_7 \cdot H_2O$) were added to the above metallic salt solution to completely complex these metal ions, then using ammonia regulates the pH of the solution to 6. The transparent solution was vigorously stirred at room temperature for 2 h. They were further continually stirred at 120 °C until transparent and viscous gel formed. The resulting gel was dried for 10 h at 180 °C and obtained black gray precursor was crushed, and calcined at 700 °C for 5 h with a heating speed of 5 °C min^{-1} under oxygen flow and then cooled down to room temperature naturally. $LaNiO_3$/NiO sample were synthesized using the same sol-gel method according to the molar ratio of 1:1+x for $La(NO_3)_3 \cdot 6H_2O$ and $Ni(NO_3)_2 \cdot 6H_2O$. NiO nanoparticles were synthesized using the same sol-gel method and the black precursor was crystallized at 700 °C in air for 5 h. $LaNiO_3$ + NiO sample was mechanically mixed according to the mass ratio of 8:1 for perovskite $LaNiO_3$ and NiO.

Physicochemical Characterizations: X-ray diffraction (XRD) measurements were carried out on Rigaku D/Max-2400 diffractometer with Cu Kα radiation (λ = 0.1542 nm) under a constant voltage of 40 kV. Transmission electron microscopy (TEM), high-resolution TEM (HR-TEM) pictures and EDX mapping of samples were obtained on a Tecnai G2 F30 filed emission transmission electron microscopy. Atomic-scale STEM images were recorded on a probe aberration-corrected STEM (Cubed Titan G2 60-300, FEI, USA) operated at 300 kV. X-ray photoelectron spectroscopy (XPS) analysis was made with a Kratos Axis Supra device and the data obtained was corrected with C 1s line at 284.8 eV. Inductively coupled plasma optical emission spectrometry (ICP-OES) analyses were performed on a Plasma Quant PQ9000 ICP spectrometer. Inductively coupled plasma mass spectrometry (ICP-MS) analyses were performed on an iCAPQc spectrometer. (BET) analyses were performed on an ASAP2020M & TriStar3020. Synchrotron radiation X-ray absorption fine structure (XAFS) spectroscopy at the Ni K-edge was acquired in transmission mode using a Si (111) double-crystal monochromator at the 1W1B station of the Beijing Synchrotron Radiation Facility (BSRF). The pressure dependent resistivity and conductivity using conventional four-probe technique measurements were conducted on a ST2258C Resistivity Tester. Raman spectroscopy measurements were conducted on a LabRAM HR Evolution spectrophotometer with 473 nm wavenumber of the excitation light source.

Electrochemical measurements: Electrochemical experiments were performed in fresh KOH on a CHI-760E Electrochemical Workstation (CHI Instruments) typical using a standard three-electrode system, while the high current stability tests were conducted in a four-electrode setup. Before the electrochemical measurement, the electrolyte was degassed by bubbling oxygen for at least 30 min to achieve a saturation condition of oxygen gas. All electrochemical investigations were performed at 25 °C using a Hg/HgO as reference electrode, a Pt plate as counter electrode, and a 3 mm diameter of glassy carbon electrode holder coated with catalyst was used as the working electrode in 1 M KOH unless otherwise specified.

Catalyst (4 mg) and carbon black (1 mg) were dissolved in mixture solvent (1970 µL, deionized water: isopropyl alcohol = 3:1) and Nafion (30 µL, 5 wt%, Sigma Aldrich) ultrasound at 25 °C for 1 h to get the catalyst dispersion. Using a pipetting gun, evenly drop the catalyst dispersion liquid onto glassy carbon electrode, drop it several times to ensure depositing of 0.2 mg cm^{-2}, leave overnight to dry naturally for later use. To directly reflect the intrinsic behavior of the catalyst by measuring the reaction current, infrared correction is applied to eliminate the effect of ohmic resistance unless otherwise stated.[52,53]

Cyclic voltammetry (CV) measurements set 10 mV s^{-1} for peroxidation tests and 5 mV s^{-1} for averaging the positive-going and negative-going scan to obtain linear sweep voltammetry (LSV) plots. In situ Raman spectra were investigated using a customized cell, with a saturated Ag/AgCl reference electrode and a Pt ring counter electrode in 1 M KOH. And the electrochemical impedance spectroscopy (EIS) tests were performed at open-circuit potentials in the frequency range of 0.01 – 100 kHz in 1 M KOH. Before in situ Raman and quasi-operando XPS tests, the carbon paper electrode holder coated with catalyst were carried out at a specially appointed potential for 20 min to obtain the surface chemical composition and structural information of materials.

The specific capacity was calculated by the equation below:

$$\eta = a + b \times log j$$

Where η stands for the overpotential, b stands for the Tafel slope, j stands for the current density.

Calculated electrochemical active surface area:

$$A_{ECSA} = C_{dl} \times 1000/40\ cm^2$$

Calculation Setup: To study the formation and electrochemical performances of heterostructures, DFT calculations within CASTEP package shave been applied to investigate the electronic structures and energetic trends.[54] For all the calculations, we have selected the generalized gradient approximation (GGA) with Perdew-Burke-Ernzerhof (PBE) for the description of the exchange-correlation interactions.[55-57] In this work, the plane-wave basis cut off energy has been set to 380 eV with the ultrasoft pseudo potentials for all the geometry optimizations. Meanwhile, the Broyden-Fletcher-Goldfarb-Shannon (BFGS) algorithm has been utilized in this work.[58] The coarse quality of k-points is applied for all the energy minimizations. The DFT models are built based on the TEM results of experiments. For $LaNiO_3$/NiO, we have cleaved (100) surfaces from both $LaNiO_3$ and NiO lattice structures with six- and five-layer thickness, respectively, to achieve the maximum match of the lattice structure and form the stable interface. This is consistent experimental characterizations, where the {100}NiO//{100}$LaNiO_3$ are formed as the interface of $LaNiO_3$/NiO. For La_2O_3, the lattice structure is also cleaved from the (100) surface with four-layer thickness to form the La_2O_3/$LaNiO_3$/NiO and La_2O_3/NiO. To guarantee the sufficient relaxation of the intermediate on the surface, we have introduced a 20 Å vacuum in the z-axis for all the models. For all the geometry optimizations of the heterostructures, the following convergence criteria have been set including the Hellmann-Feynman forces should not exceed 0.001 eV/Å, and the total energy difference and the inter-ionic displacement should be less than 5×10^{-5} eV/atom and 0.005 Å, respectively.

ASSOCIATED CONTENT

Supporting Information

This material is available free of charge via the Internet at http://pubs.acs.org. Detailed methods and additional XAS, XRD, XPS, TEM, HAADF-STEM and electrochemical data (PDF).

AUTHOR INFORMATION

Corresponding Authors

Bolong Huang − Department of Applied Biology and Chemical Technology, The Hong Kong Polytechnic University, Hung Hom, Kowloon, Hong Kong SAR, China; E-mail: bhuang@polyu.edu.hk

Pinxian Xi − State Key Laboratory of Applied Organic Chemistry, Key Laboratory of Nonferrous Metal Chemistry and Resources Utilization of Gansu Province, College of Chemistry and Chemical Engineering, Lanzhou University, Lanzhou 730000, China; E-mail: xipx@lzu.edu.cn

Authors

Yicheng Wei − State Key Laboratory of Applied Organic Chemistry, Key Laboratory of Nonferrous Metal Chemistry and Resources Utilization of Gansu Province, College of Chemistry and Chemical Engineering, Lanzhou University, Lanzhou 730000, China

Yao Zheng − School of Chemical Engineering and Advanced Materials, The University of Adelaide, Adelaide, South Australia, Australia

Yang Hu − State Key Laboratory of Applied Organic Chemistry, Key Laboratory of Nonferrous Metal Chemistry and Resources Utilization of Gansu Province, College of Chemistry and Chemical Engineering, Lanzhou University, Lanzhou 730000, China
Mingzi Sun − Department of Applied Biology and Chemical Technology, The Hong Kong Polytechnic University, Hung Hom, Kowloon, Hong Kong SAR, China
Pengfei Da − State Key Laboratory of Applied Organic Chemistry, Key Laboratory of Nonferrous Metal Chemistry and Resources Utilization of Gansu Province, College of Chemistry and Chemical Engineering, Lanzhou University, Lanzhou 730000, China
Chun-Hua Yan − State Key Laboratory of Applied Organic Chemistry, Key Laboratory of Nonferrous Metal Chemistry and Resources Utilization of Gansu Province, College of Chemistry and Chemical Engineering, Lanzhou University, Lanzhou 730000, China
Beijing National Laboratory for Molecular Sciences, State Key Laboratory of Rare Earth Materials Chemistry and Applications, PKU-HKU Joint Laboratory in Rare Earth Materials and Bioinorganic Chemistry, College of Chemistry and Molecular Engineering Peking University, Beijing 100871, China

Author Contributions

[#]Y. W., Y. Zh., and Y. H. contributed equally.

Conflicts of interest
There are no conflicts to declare

ACKNOWLEDGMENT

We acknowledge support from the National Natural Science Foundation of China (No. 21931001, 21922105, 21771156), the National Key R&D Program of China (2021YFA1501101), Special Fund Project of Guiding Scientific and Technological Innovation Development of Gansu Province (2019ZX-04), and the 111 Project (B20027). B.H. acknowledges the support of the NSFC/RGC Joint Research Scheme Project (N_PolyU502/21), and the funding for Projects of Strategic Importance of The Hong Kong Polytechnic University (Project Code: 1-ZE2V). J.Y. acknowledges the support of the National Postdoctoral Program for Innovative Talents (BX20200157). Y.Z. acknowledges funding from the Australian Research Council (DP190103472 and FT200100062).

REFERENCES

(1) Seh, Z. W.; Kibsgaard, J.; Dickens, C. F.; Chorkendorff, I.; Nørskov, J. K.; T. Jaramillo, F. Combining theory and experiment in electrocatalysis: Insights into materials design. *Science* **2017**, *355*, eaad4998.
(2) Larcher, D.; Tarascon, J. M. Towards Greener and More Sustainable Batteries for Electrical Energy Storage. *Nat. Chem.* **2015**, *7*, 19−29.
(3) Hu, C.; Zhang, L.; Gong, J. Recent progress made in the mechanism comprehension and design of electrocatalysts for alkaline water splitting. *Energy Environ. Sci.* **2019**, *12*, 2620−2645.
(4) Chen, L. F.; Feng, Y.; Liang, H. W.; Wu, Z. Y.; Yu, S. H. Macroscopic-Scale Three-Dimensional Carbon Nanofiber Architectures for Electrochemical Energy Storage Devices. *Adv. Energy Mater.* **2017**, *7*, 1700826.
(5) Jin, J.; Yin, J.; Liu, H.; Huang, B.; Hu, Y.; Zhang, H.; Sun, M.; Peng, Y.; Xi, P.; Yan, C.-H. Atomic Sulfur Filling Oxygen Vacancies Optimizes H Absorption, Boosts Hydrogen Evolution Reaction in Alkaline Media. *Angew. Chem. Int. Ed.* **2021**, *133*, 14236−14242.
(6) Suen, N.; Hung, S.; Quan, Q.; Zhang, N.; Xu, Y.; Chen, H. Electrocatalysis for the oxygen evolution reaction: recent development and future perspectives. Chem. *Soc. Rev.***2017**, *46*, 337.
(7) Sultan, S.; Ha, M.; Kim, D. Y.; Tiwari, J. N.; Myung, C. W.; Meena, A.; Shin, T. J.; Chae, K. H.; Kim, K. S. Superb water splitting activity of the electrocatalyst $Fe_3Co(PO_4)_4$ designed with computation aid. *Nat. Commun.* **2019**, *10*, 5195.
(8) Suen, N.-T.; Hung, S.-F.; Quan, Q.; Zhang, N.; Xu, Y.-J.; Chen. H. M. Chem. Electrocatalysis for the oxygen evolution reaction: recent development and future perspectives. *Soc. Rev.* **2017**, *46*, 337.
(9) Wu, T.; Sun, S.; Song, J.; Xi, S.; Du, Y.; Chen, B.; Sasangka, W. A.; Liao, H.; Gan, C. L.; Scherer, G. G.; Zeng, L.; Wang, H.; Li, H.; Grimaud, A.; Xu, Z. J. Iron-facilitated dynamic active-site generation on spinel $CoAl_2O_4$ with self-termination of surface reconstruction for water oxidation. *Nature Catalysis* **2019**, *2*, 763−772.
(10) Zhao, S.; Tan, C.; He, C.-T.; An, P.; Xie, F.; Jiang, S.; Zhu, Y.; Wu, K.-H.; Zhang, B.; Li, H.; Zhang, J.; Chen, Y.; Liu, S.; Dong, J.; Tang, Z. Structural Transformation of Highly Active Metal-Organic Framework Electrocatalysts During the Oxygen Evolution Reaction. *Nat. Energy* **2020**, *5*, 881−890.
(11) An, L.; Wei, C.; Lu, M.; Liu, H.; Chen, Y.; Scherer, G. G.; Fisher, A. C.; P.; Xi, Z. J.; Xu, Yan, C. -H. Recent Development of Oxygen Evolution Electrocatalysts in Acidic Environment. *Adv. Mater.* **2021,** 2006328.
(12) Wei, Y.; Weng, Z.; Guo, L.; An, L.; Yin, J.; Sun, S.; Da, P.; Wang, R.; Xi, P.; Yan, C. -H. Activation Strategies of Perovskite-type Structure for Applications in Oxygen-Related Electrocatalysts. *Small Methods* **2021,** 2100012.
(13) Vojvodic, A.; Nørskov, J. K. Optimizing perovskites for the water-splitting reaction. *Science* **2011**, *334*, 1355.
(14) Suntivich, J.; Gasteiger, H. A.; Yabuuchi, N.; Nakanishi, H.; Goodenough, J. B.; Shao-Horn, Y. Design principles for oxygen-reduction activity on perovskite oxide catalysts for fuel cells and metal–air batteries. *Nat. Chem.* **2011**, *3*, 546.
(15) Tseung, A. C. C.; Jasem, S. Oxygen evolution on semiconducting oxides. *Electrochim. Acta* **1977**, *22*, 31.
(16) Lee, Y. -L.; Kleis, J.; Rossmeisl, J.; Shao-Horn, Y.; Morgan, D. Prediction of solid oxide fuel cell cathode activity with first-principles descriptors. *Energy Environ. Sci.* **2011**, *4*, 3966.
(17) Fabbri, E.; Schmidt, T. J. Oxygen Evolution Reaction−The Enigma in Water Electrolysis. *ACS Catal.* 2018, *8*, 9765−9774.
(18) Fabbri, E.; Nachtegaal, M.; Binninger, T.; Cheng, X.; Kim, B. J.; Durst, J.; Bozza, F.; Graule, T.; Schaublin, R.; Wiles, L.; Pertoso, M.; Danilovic, N.; Ayers, K. E.; Schmidt, T. J. Dynamic surface selfreconstruction is the key of highly active perovskite nano-electrocatalysts for water splitting. *Nat. Mater.* 2017, *16*, 925.
(19) Sun, Y.; Li, R.; Chen, X.; Wu, J.; Xie, Y.; Wang, X.; Ma, K.; Wang, L.; Zhang, Z.; Liao, Q.; Kang, Z.; Zhang, Y. A-Site Management Prompts the Dynamic Reconstructed Active Phase of Perovskite Oxide OER Catalysts. *Adv. Energy Mater.* **2021**, *11*, 2003755.
(20) May, K. J.; Carlton, C. E.; Stoerzinger, K. A.; Risch, M.; Suntivich, J.; Lee, Y. -L.; Grimaud, A.; Shao-Horn, Y. Influence of oxygen evolution during water oxidation on the surface of perovskite oxide catalysts. *J. Phys. Chem. Lett.* **2012**, *3*, 3264.
(21) Xu, Z. J. Transition metal oxides for water oxidation: All about oxyhydroxides? *Sci. China Mater.* **2019**, *63*, 3−7.
(22) Bergmann, A.; Jones, T. E.; Moreno, E. M.; Teschner, D.; Chernev, P.; Gliech, M.; Reier, T.; Dau, H.; Strasser, P. Unified structural motifs of the catalytically active state of Co(oxyhydr)oxides during the electrochemical oxygen evolution reaction. *Nat. Catal.* **2018**, *1*, 711−719.
(23) Fabbri, E.; Nachtegaal, M.; Binninger, T.; Cheng, X.; Kim, B. -J.; Durst, J.; Bozza, F.; Graule, T.; Schäublin, R.; Wiles, L.; Per-

toso, M.; Danilovic, N.; Ayers, K. E.; Schmidt, T. J. Dynamic surface self-reconstruction is the key of highly active perovskite nano-electrocatalysts for water splitting. *Nat. Mater.* **2017**, *16*, 925–931.
(24) Kattel, S.; Liu, P.; Chen, J. G. G. Tuning Selectivity of CO_2 Hydrogenation Reactions at the Metal/Oxide Interface. *J. Am. Chem. Soc.* **2017**, *139*, 9739−9754.
(25) Wang, X.; Pan, Z.; Chu, X.; Huang, K.; Cong, Y.; Cao, R.; Sarangi, R.; Li, L.; Li, G.; Feng, S. Atomic-Scale Insights into Surface Lattice Oxygen Activation at the Spinel/Perovskite interface of $Co_3O_4/La_{0.3}Sr_{0.7}CoO_3$. *Angew. Chem. Int. Ed.* **2019**, *58*, 1−7.
(26) Tsvetkov, N.; Lu, Q.; Sun, L.; Crumlin, E. J.; Yildiz, B. Improved chemical and electrochemical stability of perovskite oxides with less reducible cations at the surface. *Nat. Mater.* **2016**, *15*, 1010−1016.
(27) Garcia-Barriocanal, J.; Rivera-Calzada, A.; Varela, M.; Sefrioui, Z.; Iborra, E.; Leon, C.; Pennycook, S. J.; Santamaria, J. Colossal ionic conductivity at interfaces of epitaxial ZrO_2: $Y_2O_3/SrTiO_3$ heterostructures. *Science* **2008**, *321*, 676−680.
(28) Chen, D.; Chen, C.; Baiyee, Z. M.; Shao, Z.; Ciucci, F. Nonstoichiometric Oxides as Low-Cost and Highly-Efficient Oxygen Reduction/Evolution Catalysts for Low-Temperature Electrochemical Devices. *Chem. Rev.* **2015**, *115*, 9869−9921.
(29) Sengodan, S.; Ju, Y-W.; Kwon, O.; Jun, A.; Jeong, H. Y.; Ishihara, T.; Shin, J.; Kim, G. Self-Decorated MnO Nanoparticles on Double Perovskite Solid Oxide Fuel Cell Anode by in Situ Exsolution. *ACS Sustainable Chem. Eng.* **2017**, *5*, 9207−9213.
(30) Gao, Y.; Chen, D.; Saccoccio, M.; Lu, Z.; Ciucci, F. From material design to mechanism study: Nanoscale Ni exsolution on a highly active A-site deficient anode material for solid oxide fuel cells. *Nano Energy* **2016**, *27*, 499−508.
(31) Feldhoff, A.; Arnold, M.; Martynczuk, J.; Gesing, Th. M.; Wang, H. The sol–gel synthesis of perovskites by an EDTA/citrate complexing method involves nanoscale solid state reactions. *Solid State Sciences* **2008**, *10*, 689−701.
(32) Chen, P.; Xu, S. Y.; Zhou, W. Z.; Ong, C. K.; Cui, D. F. n situ reflection high-energy electron diffraction observation of epitaxial $LaNiO_3$ thin films. *J. Appl. Phys.* **1999**, *85*, 3000.
(33) Disa, A. S.; Walker, F. J.; Ismail-Beigi, S.; Ahn, C. H. Research Update: Orbital polarization in $LaNiO_3$-based heterostructures. *Appl. Mater.* **2015**, *3*, 062303
(34) Ohta, H.; Hirano, M.; Nakahara, K.; Maruta, H.; Tanabe, T.; Kamiya, M.; Kamiya, T.; Hosono, H. Fabrication and photoresponse of a pn-heterojunction diode composed of transparent oxide semiconductors, p-NiO and n-ZnO. *Appl. Phys. Lett.* **2003**, *83*, 1029.
(35) Colliex, C.; Manoubi, T.; Ortiz, C. Electron-energy-loss-spectroscopy near-edge fine structures in the iron-oxygen system. *Phys. Rev. B* **1991**, *44*, 11402.
(36) Zhu, Y. M.; Do, T. H.; Tra, V. T.; Yu, R.; Chu, Y. –H.; Zhan, Q. Atomic Heterointerfaces and Electrical Transportation Properties in Self-Assembled $LaNiO_3$–NiO Heteroepitaxy. *Adv. Mater. Interfaces* 2018, 1701202.
(37) She, S. X.; Yu, J.; Tang, W. Q.; Zhu, Y. L.; Chen, Y. B.; Sunarso, J.; Zhou, W.; Shao, Z. P. Systematic Study of Oxygen Evolution Activity and Stability on $La_{1-x}Sr_xFeO_{3-\delta}$ Perovskite Electrocatalysts in Alkaline Media. *ACS Appl. Mater. Interfaces.* 2018, 10, 11715−11721.
(38) Mickevicius. S.; Grebinskij, S.; Bondarenka, V.; Vengalis, B.; Sliuzien, K.; Orlowski, B. A.; Osinniy, V.; Drube, W. Investigation of epitaxial $LaNiO_{3-x}$ thin films by high-energy XPS. *J. Alloys Compd.* **2006**, *423*, 107−111.
(39) An, L.; Huang, B.; Zhang, Y.; Wang, R.; Zhang, N.; Dai, T.; Xi, P.; Yan, C. -H. Interfacial Defect Engineering for Improved Portable Zinc–Air Batteries with a Broad Working Temperature. *Angew. Chem. Int. Ed.* **2019**, *58*, 9459−9463.
(40) Karvonen, L.; Valkeapaä, M.; Liu, R.-S.; Chen, J.-M.; Yamauchi, H.; Karppinen, M. O-K and Co-L XANES Study on Oxygen Intercalation in Perovskite $SrCoO_{3-\delta}$. *Chem. Mater.* **2010**, *22*, 70−76.
(41) Sarma, D. D.; Rader, O.; Kachel, T.; Chainani, A.; Mathew, M.; Holldack, K.; Gudat, W.; Eberhardt, W. Contrasting behavior of homovalent-substituted and hole-doped systems: O K-edge spectra from (M = Mn, Fe, and Co) and $La_{1-x}Sr_xMnO_3$. *Phys. Rev. B* **1994,** *49*, 14238.
(42) Wang, X.; Huang, K.; Yuan, L.; Li, S.; Ma, W.; Liu, Z.; Feng. S. Molten Salt Flux Synthesis, Crystal Facet Design, Characterization, Electronic Structure, and Catalytic Properties of Perovskite Cobaltite. *ACS Appl. Mater. Interfaces* **2018**, *10*, 28219−28231.
(43) Yin, J.; Jin, J.; Lu, M.; Huang, B.; Zhang, H.; Peng, Y.; Xi, P.; Yan. C. -H. Iridium Single Atoms Coupling with Oxygen Vacancies Boosts Oxygen Evolution Reaction in Acid Media. *J. Am. Chem. Soc.* **2020**, *142,* 18378−18386.
(44) Bak, J.; Bae, H. B.; Chung, S. -Y. Investigation of epitaxial $LaNiO_{3-x}$ thin films by high-energy XPS. *Nat. Commun.* **2019**, *10*, 2713.
(45) Lacorre, P.; Torrance, J. B.; Pannetier, J.; Nazzal, A. I.; Wang, P. W.; Huang, T. C. Synthesis, crystal structure, and properties of metallic $PrNiO_3$: comparison with metallic $NdNiO_3$ and semiconducting $SmNiO_3$. *J. Solid State Chem.* **1991**, *91*, 225−237.
(46) Stevens, M. B.; Enman, L. J.; Batchellor, Adam. S.; Cosby, M. R.; Vise, A. E.; Trang, C. D. M.; Boettcher, S. W. Measurement techniques for the study of thin film heterogeneous water oxidation electrocatalysts. *Chem. Mater.* **2017** *29*, 120−140.
(47) Hepting, M.; Kukuruznyak, D.; Benckiser, E.; Le Tacon, M.; Keimer, B. Raman light scattering on ultra-thin films of $LaNiO_3$ under compressive strain. *Physica B: Condensed Matter* **2015**, *460*, 196−198.
(48) Chen, X. X. D.; Zhao, B.; Mahmoud, M. A.; El-Sayed, M. A.; Liu, M. Probing Structural Evolution and Charge Storage Mechanism of NiO_2H_x Electrode Materials using In Operando Resonance Raman Spectroscopy. *Adv. Sci.* **2016**, *3*, 1500433.
(49) Louie, M. W.; Bell, A. T. An investigation of thin-film Ni–Fe oxide catalysts for the electrochemical evolution of oxygen. *J. Am. Chem. Soc.* **2013**, *135*, 12329−12337.
(50) Hu, W.; Liu, Y.; Withers, R. L.; Frankcombe, T. J.; Noren, L.; Snashall, A.; Kitchin, M.; Smith, P.; Gong, B.; Chen, H.; Schiemer, J.; Brink, F.; Wong-Leung, J. Electron-pinned defect-dipoles for highperformance colossal permittivity materials. *Nat. Mater.* **2013**, *12*, 821−826.
(51) Zou, Q.; Ruda, H.; Yacobi, B. G.; Farrell, M. Microstructural characterization of donor-doped lead zirconatetitanate films prepared by sol−gel processing. *Thin Solid Films* **2002**, *402*, 65−70.
(52) Yin, J.; Li, Y.; Lv, F.; Lu, M.; Sun, K.; Wang, W.; Wang, L.; Cheng, F.; Li, Y.; Xi, P.; Guo. S. Oxygen Vacancies Dominated NiS_2/CoS_2 Interface Porous Nanowires for Portable Zn–Air Batteries Driven Water Splitting Devices. *Adv. Mater.* **2017**, *29*, 1704681.
(53) An, L.; Feng, J.; Zhang, Y.; Wang, R. Liu, H.; Wang, G. –C.; Cheng, F.; Xi, P. Epitaxial Heterogeneous Interfaces on N-Ni-MoO_4/NiS_2 Nanowires/Nanosheets to Boost Hydrogen and Oxygen Production for Overall Water Splitting. *Adv. Funct. Mater.* **2019**, *29*, 1805298.
(54) Clark, S. J.; Segall, M. D.; Pickard, C. J.; Hasnip, P. J.; Probert, M. J.; Refson, K.; Payne, M. C. First Principles Methods Using Castep. *Zeitschrift Fur Kristallographie* **2005**, *220*, 567−570.
(55) Perdew, J. P.; Burke, K.; Ernzerhof, M. Generalized Gradient Approximation Made Simple. *Phys. Rev. Lett.* **1996**, *77*, 3865−3868.
(56) Hasnip, P. J.; Pickard, C. J. Electronic Energy Minimisation with Ultrasoft Pseudopotentials. *Comput. Phys. Commun.* **2006**, *174*, 24−29.

(57) Perdew. J. P.; Chevary, J. A.; Vosko; S. H.; Jackson, K. A.; Pederson, M. R.; Singh, D. J.; Fiolhais, C. Atoms, Molecules, Solids, and Surfaces: Applications of the Generalized Gradient Approximation for Exchange and Correlation. *Physical Review B* **1992**, *46*, 6671−6687.

(58) Head, J. D.; Zerner, M. C. A Broyden-Fletcher-Goldfarb-Shanno Optimization Procedure for Molecular Geometries. *Chem Phys Lett* **1985***, 122*, 264−270.

TOC